Growth of ultrathin cobalt oxide films on Pt(111)

Maurizio De Santis,[1,2,*] Andreas Buchsbaum,[1] Peter Varga,[1] and Michael Schmid[1]
[1]*Institut für Angewandte Physik, Technische Universität Wien, A-1040 Wien, Austria*
[2]*Institut Néel, CNRS and UJF, BP 166, F-38042 Grenoble Cedex 9, France*
(Received 6 June 2011; published 12 September 2011)

Cobalt surface oxides were grown on Pt(111) by depositing Co and dosing with molecular oxygen at temperatures ranging between 300 and 740 K. Oxidation of 1 monolayer (ML) Co results in a two-dimensional (2D) moiré structure, observed using both low-energy electron diffraction and scanning tunneling microscopy and interpreted as a polar (oxygen terminated) CoO(111) atomic bilayer. It is expanded by $2.7 \pm 0.6\%$ in the surface plane with respect to bulk CoO. An almost-flawless moiré pattern is obtained after a final step of annealing at 740 K in oxygen. Insufficient oxidation leads to defects in the moiré pattern, consisting of triangular dislocation loops of different sizes; the smaller ones occupy half of the moiré cell. Low-temperature annealing (450 K) can be used to create a zigzag phase, which is mainly observed in 1-ML-thick areas after several cycles of Co deposition (1 ML each) and oxidation at 10^{-7} mbar. The CoO films obtained by deposition/oxidation cycles exhibit Stranski-Krastanov growth; the structure of the 2D layer between the islands depends on the thermal treatment. It exhibits the moiré pattern after annealing at 740 K, whereas the zigzag phase was observed after low-temperature annealing. The second monolayer consists of a moiré pattern different from that of the first layer, presumably a wurtzite-like structure. Above the third layer, we observe only small three-dimensional islands, which exhibit a bandgap. We have also studied oxidation of surface alloys obtained by depositing Co and annealing. On these surfaces, we found a quasi-(3×3) reconstruction. Structure models are presented for all phases observed, and we argue that some of the moirélike structures might be useful as templates for metal cluster growth.

DOI: 10.1103/PhysRevB.84.125430 PACS number(s): 68.47.Gh, 68.37.Ef, 68.55.J−, 68.55.A−

I. INTRODUCTION

Ultrathin transition metal oxide (TMO) films are investigated mainly for their catalytic[1,2] and magnetic[3] properties. For the latter, the most important domain of application is the exploitation of exchange anisotropy or exchange bias occurring at the interface between antiferromagnetic oxides and ferromagnets.[4] Such exchange interaction systems are employed in spin valves and in systems showing giant magnetoresistence. A further interesting effect of exchange bias is to overcome the superparamagnetic limit in nanostructures, as it happens for Co nanoparticles embedded in a CoO matrix.[5] In all these applications, a key parameter for enhancing the exchange interaction is the control of the interface structure at the atomic level, which determines the strength of the exchange coupling.[3]

CoO/Co bilayers reveal an extremely strong exchange bias[6] and are interesting for both fundamental studies and applications. Bulk CoO is antiferromagnetic with a Néel temperature T_N of 293 K and a large magnetic anisotropy.[3] Larger Néel temperatures were obtained in rather thick CoO/NiO superlattices,[7] at the price of a reduction of the anisotropy. A higher Néel temperature than CoO was also observed for shorter-period superlattices, 3 monolayer (ML) CoO + 3 ML NiO, coupled to an ultrathin ferromagnetic PtCo(111) layer, as evidenced by the observation of exchange bias up to ∼320 K in this system.[8] Above this temperature, the interfacial CoO is polarized by the PtCo layer and contributes to the total ferromagnetic signal. Again, the knowledge of the structure of the buried interface is fundamental in the understanding of such phenomena.

Similar to alumina films,[9,10] the large supercells of epitaxial ultrathin TMO films grown on metals are used as templates for self-assembling arrays of metal nanoclusters, as shown in the cases of the moiré or zigzag pattern resulting from the growth of a single FeO bilayer on Pt(111)[11,12] and TiO_x/Pt(111),[13] as well as the (4×4) vanadium oxide mesh on Pd(111).[14] These applications require understanding of the surface structure of the oxide films.

At room temperature (RT), CoO has the rocksalt crystal structure, with the lattice constant $a_{CoO} = 425.4$ pm.[7] Each (111) plane contains one kind of atoms only, Co or O, disposed in an hexagonal mesh with the in-plane interatomic distance of 301 pm. Below T_N, it orders with parallel spins on (111) planes and with antiparallel spin directions on adjacent (metal) planes. The CoO(111) surface thus exhibits the largest density of uncompensated spins and hence *a priori* the largest exchange interaction. Unfortunately, this surface is polar; thus, the calculated (111) surface energy for the bulk material is infinite.[15,16] This divergence can be suppressed by various mechanisms,[17] e.g., surface reconstructions,[18] a crystallographic structure at the surface different from that in the bulk,[19] vacancy islands,[20] reduced charge of the surface ions,[21] nonstoichiometric surfaces,[22] or adsorbates.[23] For ultrathin films, the polar surface problem is alleviated; nevertheless, it reduces the stability of the films, making it difficult to achieve layer-by-layer growth of well-ordered CoO(111) films.

The structure of ultrathin epitaxial CoO films on several substrates, e.g., Ir(100)[24] and Pd(100),[25] was already studied, mainly by scanning tunneling microscopy (STM) and low-energy electron diffraction (LEED). The growth of cobalt oxide on Pt(111) at RT was investigated employing reflection high-energy electron diffraction and spectroscopic techniques.[26] It was reported that cycles of alternate Co deposition (1 ML) and O_2 dosing (300 langmuir, or L) at

 ©2011 American Physical Society

RT results in a nonreconstructed CoO(111) film, described as rather flat up to 6 ML. Our STM results are more sensitive to the roughness, which indeed occurs already at the beginning of the growth.

Here, we present a detailed study in a large temperature range of the first growing stages of this oxide, combining STM, LEED, and Auger electron spectroscopy (AES). Several surface cobalt oxide phases were found, depending on the preparation.

II. EXPERIMENTAL AND METHODS

The Pt(111) substrate was prepared by cycles of 2 keV Ar^+ sputtering and annealing at ~1070 K in an ultrahigh vacuum (UHV) chamber with a base pressure in the low 10^{-10} mbar range. At this stage, no impurities could be detected by AES. Co was deposited from a pure rod using a liquid-nitrogen-cooled electron-beam evaporator. During deposition, a retarding voltage was applied to the end of the evaporator to suppress high-energy metal ions, which could modify the growth.[27] The deposition rate, calibrated with a quartz crystal microbalance, was typically 1/3 ML per minute, where we define 1 ML as the number of atoms in a Pt(111) monolayer.

The film was annealed without oxygen at different temperatures (leading to alloying at high T). Unless specified otherwise, the oxide was formed by dosing molecular oxygen at $\sim 10^{-7}$ mbar for 10 min., resulting in an exposure to 50 ± 10 L (1 L corresponds to a dosage of 10^{-6} torr $\times$ s). A large interval of the oxidation temperature was spanned during the experiments, from RT to 740 K. STM, LEED, AES, and low-energy ion scattering (LEIS) measurements were performed in a connected UHV chamber, with base pressure $<5 \times 10^{-11}$ mbar. The STM measurements were performed using a customized commercial STM (Omicron μ-STM) with an electrochemically etched W tip. All STM images were obtained in constant current mode, with the voltage bias (V_s) applied to the sample. Lattice constants of moiré structures were determined by selecting the spots corresponding to either the substrate or the overlayer in the Fourier transform of STM images, doing a backtransform, and then measuring the lattice constant in the same area of the image. Because this procedure eliminates any differences of scanner calibration among different images, as well as the distortions within an image, it allows us to reach an accuracy of ~0.5%. AES spectra were collected with a cylindrical mirror analyzer with a concentric electron gun. LEIS was measured with 1 keV He^+ ions at a scattering angle of 90°.

III. RESULTS AND DISCUSSION

A. The moiré structure

As a first step, we studied the exposure to oxygen of 1 ML Co/Pt(111) as function of the temperature. Figure 1(a) shows an STM image of ~1 ML of Co deposited at RT on the substrate and then dosed with 50 L O_2 at RT (without any annealing of the as-deposited Co film). Before the oxidation, this surface was covered by large islands of monolayer thickness that coexisted with uncovered Pt regions and with areas showing a second Co layer on top of the first one.[28] In the figure,

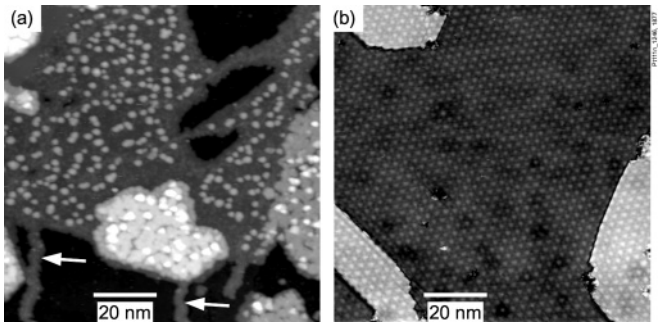

FIG. 1. STM images ($V_s = +0.5$ V, $I_t = 0.1$ nA) of 1 ML Co/Pt(111) deposited at RT and: (a) dosed with 50 L O_2; (b) annealed and dosed with O_2 at 570 K and then annealed under oxygen at 740 K. The arrows in (a) indicate two dendrites. Image processing was used in (b) to reduce the step height, making the corrugation on the terraces more apparent.

we observe small clusters, ~250 pm in height and 2 nm in size, resulting from the oxidation of previously Co-covered areas, whereas no islands appear on Pt areas (dark regions). We explain the presence of clusters with the expulsion of atoms from the underlying Co layer during oxidation: a bulk CoO(111) plane has a Co atomic density 15% lower than pseudomorphic Co/Pt(111); the difference is actually larger because of a slight contraction[28] of the as-deposited Co on the Pt(111) surface. The large dendrites formed when depositing Co submonolayers on Pt(111)[29] are also observed on the oxidized sample, shown in Fig. 1(a). These dendrites should consist mainly of Pt, and almost no clusters form on them.

An almost flawless and flat surface oxide (Fig. 1(b)) was obtained by using two different annealing temperatures: 1 ML of Co was deposited at RT and annealed at 570 K, to get a flat Co atomic layer partly alloyed with Pt; at this same temperature, O_2 was dosed (dose: 50 L); and finally, it was annealed for 10 min. at 740 K in 10^{-8} mbar O_2. The first oxidation step is performed at a temperature low enough to avoid Co diffusion into the near-surface Pt layers before an oxide forms. The second step then results in an oxide layer with a very low defect concentration. The large-scale STM of Fig. 1(b) shows a moiré pattern, which extends over the image size (100 nm) with a very low density of defects. The moiré is observed on all terraces, and its period is $\Lambda = 2.70 \pm 0.05$ nm. The interatomic distance $d_{\text{oxide}} = 309 \pm 2$ pm, obtained by atomically resolved images, is expanded by ~11% with respect to the Pt substrate (interatomic distance $d_{\text{Pt}} = 277.5$ pm). These values satisfy the moiré equation for an unrotated overlayer: $1/\Lambda = 1/d_{\text{Pt}} - 1/d_{\text{oxide}} = (2.7 \pm 0.1\ \text{nm})^{-1}$. The same misfit is observed in the LEED pattern (Fig. 2), which is homogeneous on the entire surface. Compared to bulk CoO(111), the in-plane distances are expanded by 2.7 ± 0.6%. LEIS on this same surface shows contributions mainly from Co and O atoms, the Pt peak being only a few percent of the total signal. Assuming that the Pt signal comes from uncovered Pt areas, comparison with standard spectra of pure Pt indicates that $\leqslant 1$% of the surface is pure Pt. Concerning the stoichiometry of the films, the STM images do not allow us to determine whether we have a CoO bilayer like FeO/Pt(111)[30–33] or a O-Co-O trilayer structure like the O-Rh-O surface oxide obtained by oxidation of Rh(111).[34] The latter can be excluded by AES,

FIG. 2. LEED pattern of the moiré shown in Fig. 1(b) ($E = 120$ eV).

by comparison with the film oxidized at RT (where formation of a trilayer oxide is unlikely; the perfect moiré has only a few percent higher oxygen content than the RT-oxidized film), and by comparison of AES data with those of the trilayer oxide on Rh(111).

Thus, this structure consists of a single CoO bilayer, O terminated and slightly in-plane expanded. Beside the analogy with the FeO case, this kind of termination is the only one that allows us to coherently explain the oxygen-deficient structures discussed in the next paragraphs. The expansion is similar to the value of 2% found for FeO/Pt(111).[30,32] For the FeO films, this expansion was accompanied by a strong contraction of the interlayer spacing (68 pm, compared to 125 pm in bulk[33]). Such a reduction of the interlayer distance is also likely to occur in our CoO films, decreasing the dipole moment and hence the electrostatic energy. At variance with the iron oxide case, the moiré pattern that we observe is not rotated compared to the Pt(111) surface mesh. The need for a two-step annealing process for the CoO film, not required for FeO, might be related to the higher solubility of Co in Pt as compared to Fe.[35]

Figures 3(a)–3(e) shows the moiré imaged with different bias. The registry of the images can be inferred from a few point defects (circles). Depending on the sample bias voltage, the appearance of the moiré pattern changes, which evidences the role of surface electronic states in the corrugation observed by STM. Clearly, the honeycomb feature in Figs. 3(a) and 3(b) is not related to the geometric corrugation of the moiré structure, because the atomic corrugation is strongly reduced in the bright honeycomb regions, where it seems that a smeared-out electronic state dominates tunneling. The voltage-dependent appearance of the oxide was also observed in the FeO/Pt(111) case, but was less pronounced, because there the atomic corrugation seemed to be not significantly reduced in areas of high density of states.[36] The images shown in Figs. 3(a)–3(e) were obtained on a sample with three cycles of Co deposition (1 ML each) and annealing in oxygen at 570 K, imaging the first-layer moiré pattern between the three-dimensional (3D) islands. The images of the first-layer moiré are the same for one

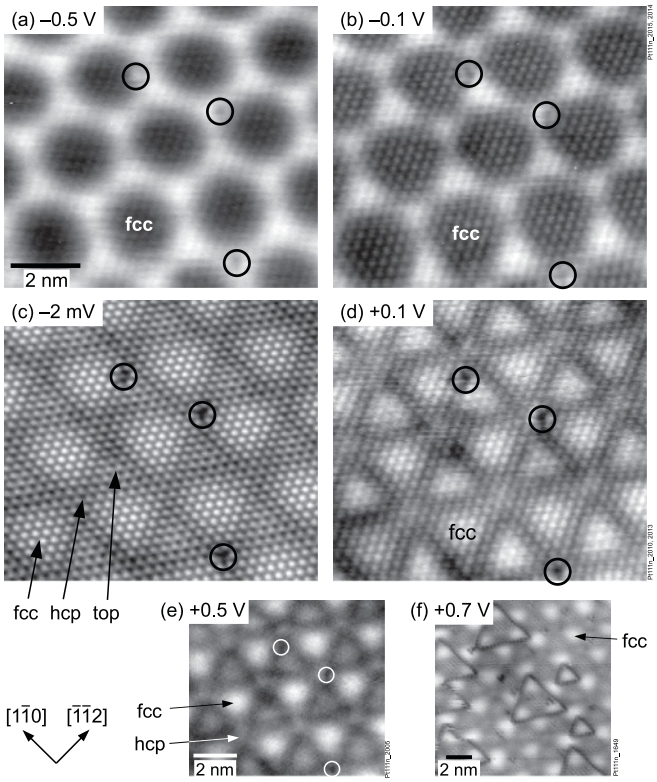

FIG. 3. STM images of the CoO/Pt(111) moiré structure. (a)–(e) The same region is imaged with different sample bias ($I_t = 1$ nA for all). Regions with Co in fcc, hcp, and on-top sites of the Pt substrate atoms are identified by comparison with images of the triangular stacking faults. (a)–(e) were obtained on the 2D layer of a sample obtained with three cycles of 1 ML Co deposition and O_2 exposure at 570 K, followed by annealing at 740 K in 1×10^{-8} mbar O_2 (see Sec. III D); circles mark the same three defects in (a)–(e). (f) Dislocation triangles (1 ML Co, 50 L O_2 at 620 K, and then annealing at 740 K; $I_t = 0.1$ nA).

or several deposition cycles, and the in-plane lattice constant is the same at 309 pm.

When comparing voltage-dependent images of this moiré structure with those of the dislocation triangles (see the next section), we can determine the stacking of the different areas in the moiré. The areas with the atoms appearing as well-defined protrusions at very low tunneling voltages (Figs. 3(c) and 4(a)) are identified as those with face-centered cubic (fcc) stacking; these areas appear dark at negative sample voltages V_s and bright at $V_s \geqslant 0.1$ V.

B. Dislocation triangles in the moiré structure

Preparation with insufficient oxidation results in a moiré pattern with a large density of triangular dislocation loops. The STM image of Fig. 4(a) was measured after deposition of 1 ML of Co on Pt(111) at RT, followed by annealing (10 min. at 640 K) and dosing O_2 (~50 L) at a temperature of 640 K, but without the postannealing in O_2 required to produce the perfect moiré structure. Within the dislocation loops, atoms at the surface follow a different stacking, as shown by the line of the arrow indicating the [1$\bar{1}$0] direction.

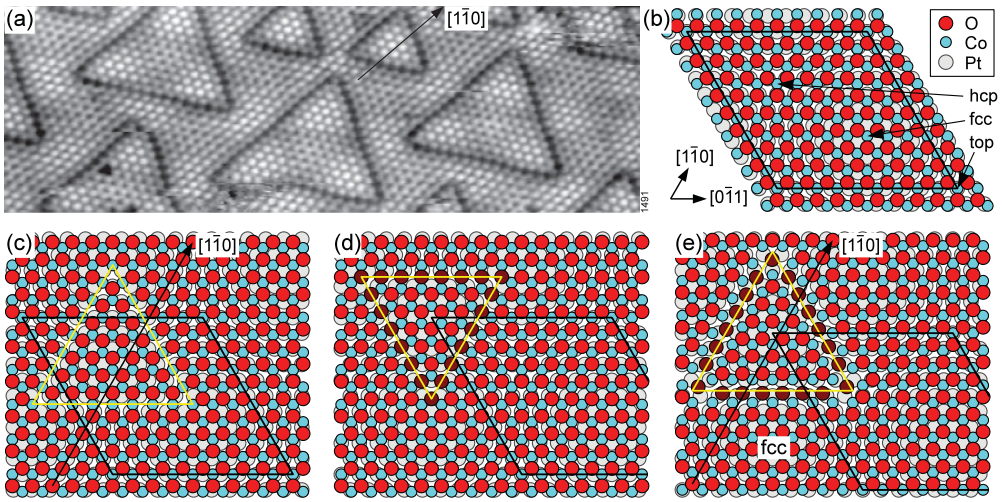

FIG. 4. (Color online) (a) 18 × 6 nm^2 STM image of 1 ML Co/Pt(111) annealed and exposed to O_2 at 640 K ($V_s = -1$ mV, $I_t = 2$ nA). (b)–(e) Ball models of the unperturbed moiré structure, and different types of triangular dislocation loops; we argue that (c) is the correct model. Oxygen atoms at the dislocations that are in asymmetric twofold or fourfold hollow sites are shown as dark (brown) filled circles.

Figure 4(b) shows a ball model of the moiré structure, with the periodicity approximated to the closest commensurate value, $\Lambda = 10\ d_{Pt}$ (2.775 nm). Co and O atoms follow the Pt(111) fcc stacking sequence *ABC* in the lower right of the moiré cell, shown in Fig. 4(b). Due to the misfit, the stacking switches to hexagonal close packed (hcp) in the upper right of the cell, whereas Co is on top of Pt at the cell corners. The twinned domain (*ACB* stacking in the registry position) would be obtained by exchanging the in-plane coordinates of Co and O. On the perfect moiré surface, this twinned domain, if it exists, cannot be present in a significant fraction of the surface, as evidenced by the threefold symmetry of the moiré spots in the LEED pattern (Fig. 2). Two domains with a similar area would result in sixfold symmetry of the LEED pattern (except for the substrate spots). Moreover, in the well-annealed moiré structure, no domain walls are observed by STM, also indicating that there is only one domain.

Merte and coworkers in the Århus group have studied similar dislocation triangles on FeO/Pt(111).[37,38] However, they created the dislocation loops by chemically reducing the perfect FeO film with atomic hydrogen, whereas the structures we observed are formed during growth. Not surprisingly, considering the method of creating these defects, Merte *et al.* have interpreted their dislocations as defects of the oxygen layer only, with the Fe layer below remaining the same as in the unperturbed moiré structure.[37,38] Their model for the small triangles visible in Fig. 4(a) is shown in Fig. 4(c); it perfectly fits our STM images under the assumption that STM shows the O atoms as calculated for FeO in Ref. 31 (in contrast to Ref. 37, we have never observed a tip change where the tip switches to imaging the other atom type as protrusions). The line in [1$\bar{1}$0] direction clearly indicates different stacking inside the triangle. For FeO, the driving force behind the formation of these defects was explained as a preference for fcc-like stacking in the upper layers (Pt-Fe-O), avoiding the regions of hcp-like stacking in the unperturbed moiré.[37]

In our case, with the structures formed by annealing a Co film in oxygen, we have to consider the possibility of a dislocation loop in the Co layer, enclosing an area with a stacking fault between the Pt and the Co layers. Such a rearrangement would be clearly favorable if it could avoid the on-top sites of Co on Pt, which may be energetically even less favorable than hcp-like stacking.[37] Next, we describe the two possible arrangements for triangular dislocation loops that avoid on-top sites. These structure models require a stacking fault between the Pt and the Co layers. We show that these models do not explain the STM image in Fig. 4(a), but one of these arrangements is the basis for understanding the "zigzag" phase in the following section.

The first of these models is shown in Fig. 4(d) (for simplicity, we consider only the small triangles here, with side lengths of ∼7 atoms). In this case, the dislocation loop would be situated only in the Co layer, while the oxygen lattice could be uninterrupted. This model would require STM to show the Co atoms as protrusions. For obtaining a reasonable atomic arrangement at the triangle boundary, we have to invert the orientation of the triangle with respect to the one observed experimentally. This can only happen if the majority of the film grows not with the same fcc stacking sequence as the Pt substrate but with twinned stacking. This must be considered unlikely, however, because the stacking fault energy of Co/Pt(111) must be rather high, as evidenced by significantly different areas of fcc and hcp Co in the first monolayer[28]; the same is expected to hold for the oxide.[37]

Assuming that the majority of the moiré is not twinned, we can create a model avoiding the on-top sites, as shown in Fig. 4(e). The oxygen atoms at the dislocations (dark in Fig. 4(e)) are in asymmetric fourfold hollow sites; thus, they would almost certainly appear different from those in the usual threefold sites, but this is not observed (this argument would be invalid, assuming that STM images show Co, however). We later show that this kind of dislocation exists in a different structure, the "zigzag" phase, and that STM indeed images the oxygen atoms. We can also exclude the model in Fig. 4(e) for another reason: The stacking sequence is the same (fcc) near the center of the triangles and immediately outside the

triangle sides (marked "fcc" in Fig. 4(e)). The STM images show a different appearance at these positions, which strongly indicates different stacking. This is true for very low tunneling voltages (Fig. 4(a)), as well as for higher voltages, where electronic effects dominate (Fig. 3(f)). Thus, there is no viable model for the triangular dislocation loops avoiding on-top Co, which means that the model in Fig. 4(c), not avoiding the on-top sites, must be the correct one.

As mentioned earlier, annealing in oxygen at 740 K removes the dislocation triangles, resulting in a well-ordered moiré. At the same time, the ratio of the AES O/Co (513/778 eV) peak-to-peak heights increases by ∼10%. This is explained by the increase of the oxygen coverage when the oxygen-deficient dislocation loops are healed. Furthermore, at this temperature, excess Co can diffuse to deeper Pt layers, below the probing depth of AES.

C. The zigzag phase

The structure of the two-dimensional (2D) layer obtained by oxidation at an even lower temperature of 450 K is quite different from the moiré. At this temperature, it is impossible to obtain sufficiently large 2D islands by depositing just 1 ML Co and annealing; thus, we have obtained the structure by two cycles of Co deposition (1 ML each) and O_2 dosing (50 L each). The first monolayer was deposited at RT, and then the sample was annealed at 450 K; oxidization and the second deposition–oxidation cycle were done at 450 K as well. Similar to the moiré structure with a large number of dislocation triangles, AES indicates an O/Co ratio ∼10% below that of the perfect moiré. An atomically resolved STM image of the phase grown at 450 K, obtained by zooming in a flat region between the 2-ML and the higher islands, is shown in Fig. 5(a). The surface appears nanostructured with parallel dark rows, spaced by ∼2.9 nm. Inside the bands delimited by these rows, the atoms are arranged in triangles, whose boundaries form a dark zigzag pattern.

The structure is observed with slightly different cell sizes; the most frequent unit cell is a rectangular $(10 \times 6\sqrt{3})$ − rect cell (2.775 × 2.884 nm^2). Assuming that STM again shows the oxygen atoms as protrusions, and using the same building blocks as discussed earlier, we can derive a model of the structure: The appearance of the long dark lines along the $[1\bar{1}0]$ direction in the STM image is similar to that of the dislocation triangles discussed earlier, with a locally rectangular arrangement of the O atoms. On the other hand, the hexagonal O lattice is only weakly disturbed at the dark zigzag lines, with one O row appearing darker, as we would expect for the structure in Fig. 4(e). The resulting structure model is shown in Fig. 5(b). This structure avoids the unfavorable on-top sites of Co that would occur in the unperturbed moiré structure. The zigzag-shaped line defects in the Co layer separate triangles with different orientations and different stacking: fcc and twinned fcc with respect to the substrate. The oxygen atoms at these line defects not only appear with different contrast (darker), as expected for their fourfold sites in contrast to the threefold sites elsewhere, but also appear frizzy in many places, indicating that the line defect jumps back and forth by one atomic row while the image is scanned. In dislocation terminology, the line defects in the Co layer are Shockley partial dislocations, which can easily glide in the (111) layer.

In the model shown in Fig. 5(b), the Co and O lattices have been modified by introducing the line defects only; further distortions have not been applied. In this figure, the areas of perfect fcc stacking are not at the center of the triangles but rather are closer to the base (the straight line defect in the O layer). The STM images of the triangular dislocation loops (Fig. 4(a)) show the highest contrast of the O atoms in regions of perfect fcc stacking (the center of the triangles), and transferring this knowledge to the zigzag structure means that here the perfect fcc stacking is actually observed closer to the center of the triangles. Thus, the Co and O atoms are slightly displaced in the direction of the arrows in Fig. 5(b). This is advantageous, especially for the atoms near the tip of the triangles, where Fig. 5(b) shows that the Pt-Co-O stacking is close to the unfavorable hcp stacking. There, shifting the CoO overlayer in the direction of the arrows makes the stacking more fcc-like. As a result of this displacement, the atomic rows become slightly wiggly, as indicated by a wavy line at the bottom of Fig. 5(b). This is also observed in the STM image, where the diagonal dark defects in the O layer are not perfectly straight but slightly wiggly. The amplitude of these wiggles as estimated from the STM image is ∼30 pm. The fcc stacking in the triangles is also confirmed by STM images at larger positive voltages (not shown), where the centers of the triangles appear brightest, similar to the fcc regions in Figs. 3(e) and 3(f).

The stoichiometry of the zigzag unit cell shown in Fig. 5(b) is $Co_{90}O_{82}$; thus, it is oxygen deficient, similar to the moiré with the triangular dislocation loops. As the cell contains 120 Pt atoms per (111) layer, the Co and O densities are 75% and 68% of the Pt density, respectively. As expected for a structure with line defects, this is less than in the defect-free moiré (81%).

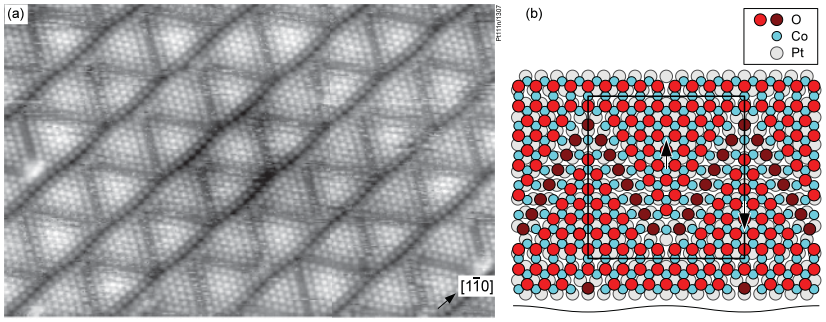

FIG. 5. (Color online) (a) STM image (28 × 12 nm^2, V_s = 10 mV, I_t = 1 nA) of the zigzag structure, obtained in a region between the islands after two cycles of Co deposition (1 ML) and O_2 dosing (50 L) at 450 K. (b) Ball model of the structure. Oxygen atoms at the zigzag dislocation line (shown darker) are in asymmetric fourfold hollow sites.

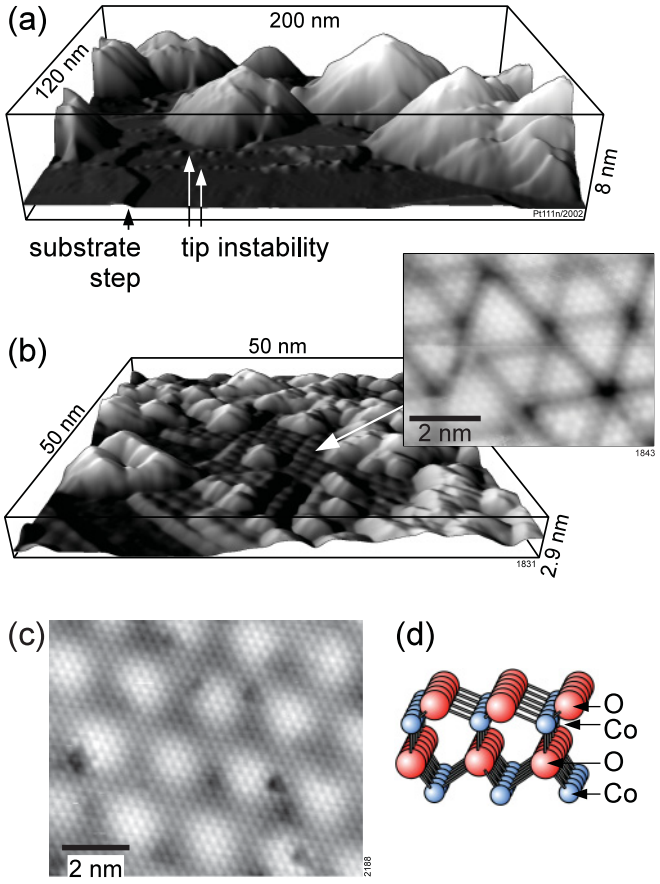

FIG. 6. (Color online) STM images of thicker films. (a) Three cycles of Co deposition (1 ML) and O_2 dosing (50 L) at 570 K, followed by annealing in oxygen at 740 K at the end ($V_s = 1.2$ V, $I_t = 0.1$ nA). (b) The same procedure at $T = 450$ K ($V_s = -1$ V, $I_t = 0.1$ nA). In both cases, the first monolayer is deposited at RT. (c) The second-layer moiré structure after depositing 1 ML Co at RT and annealing and dosing O_2 at 570 K and then 740 K. (d) Ball model of wurtzite-terminated cobalt oxide.

This structure is reminiscent of the so-called z′ phase of TiO_x/Pt(111),[39,40] even though the TiO_x/Pt(111) structure has a smaller unit cell (larger lattice constant in the oxide layer) and the zigzag rows appear bright, not dark, in the STM images of TiO_x/Pt(111). A recent model for this structure[41] is similar to ours, but with the O and metal lattices exchanged (O forms the upper layer, nevertheless). Thus, in the TiO_x/Pt(111) model, the straight line defects are in the Ti, not the O, layer, and the oxygen density exceeds the Ti density.

D. Multilayer growth

In Sec. III A, we discussed the growth and structure of an almost flawless 2D Co oxide layer on the Pt(111) surface. However, the large majority of applications require a film a few nanometers thick, exhibiting the electric and magnetic properties characteristic of the CoO bulk phase. Inspired by Ref. 26, we repeated the procedure for the moiré several times in the attempt to grow such a thicker layer. Figure 6(a) shows a large-scale STM image measured on a film prepared as follows: 1 ML Co was deposited at RT; it was annealed at 570 K and dosed with ∼50 L O_2; two further cycles of Co deposition (1 ML) and O_2 dosing (50 L) were performed, always at 570 K; and finally, it was annealed for 10 min. at 740 K in 10^{-8} mbar O_2. We observe large 3D islands, ∼5 nm high, with a 2D oxide layer between. The latter is the 2D moiré pattern of a single CoO layer (the STM images of the moiré shown in Figs. 3(a)–3(e) were collected on this sample). The image also shows many indications of tip instability, especially when scanning over the 3D islands, which indicates a semiconducting or insulating nature of the islands (cf. scanning tunneling spectroscopy data given later). We conclude that this Stranski-Krastanov growth is the thermodynamically stable configuration, and thicker flat oxide films can be obtained only by decreasing the mobility of the atoms at the surface.

We then grew CoO films following the procedure of Ref. 8, consisting also of cycles of Co deposition (1 ML) and O_2 dosing (50 L), but at a lower temperature. The first monolayer was evaporated at RT, and then the substrate temperature was increased to 450 K for annealing, oxidizing, and the following deposition/oxidation cycles. Figure 6(b) shows the STM image of the surface after three cycles. The growth is still of the Stranski-Krastanov type, but the 3D islands are significantly smaller. They are between 1 and 2 nm high and have a roughly triangular shape, with the sides oriented like the basis vectors of the Pt surface hexagonal mesh. A surface x-ray diffraction experiment performed on samples grown in the same way has shown that the islands' structure fits well with CoO(111) rocksalt nanostructures in orientational epitaxy, with bulk interatomic distances.[42]

The second monolayer (inset in Fig. 6(b)) shows a moirélike structure with many defects—partly reminiscent of the Cr/Pt(111) pinwheel[43] and the VO_x/Rh(111) "wagon wheel" [44] structures, though these are clearly different from the current case (pure metal and single oxide layers, respectively). In contrast to the first-layer CoO/Pt(111) moiré, the appearance of this second-layer structure does not significantly change with tunneling voltage. We also obtained patches of a more well-ordered form of this second-monolayer structure by the preparation leading to the perfect first-layer moiré; the second-layer structure appears in islands where Co has been expelled due to the increase of the lattice constant when forming the oxide. In this case, the second layer forms an almost-perfect moiré structure, with a supercell size between 2.3 and 2.4 nm and hardly any rotation with respect to the Pt substrate (Fig. 6(c)). This means that the lattice constant of the two-layer structure is ∼315 pm, larger than that in the first-layer moiré (309 pm; 2.7-nm supercell). Because the CoO layer forming the first-layer moiré has a lattice constant larger than bulk CoO, it would be unusual to have a two-layer oxide with the same structure but a lattice constant deviating even more from the bulk value. We therefore believe that it is a different structure—most likely a wurtzite-terminated cobalt oxide, as already observed for CoO on Ir(100)[19] (Fig. 6(d)). CoO wurtzite has the lattice constant $a_w = 324$ pm; the actual lattice constant of the two-layer structure will be an average of the rocksalt and the wurtzite ones. As in the CoO/Ir(100) case, the reason for the appearance of the wurtzite structure can be explained by the electrostatic energy: the spacing between the Co and the O planes of a bilayer is 44 pm in the wurtzite structure[45] or even lower,[46] to be compared to 123 pm in

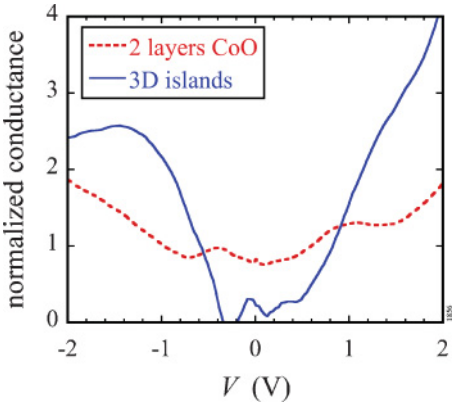

FIG. 7. (Color online) STS measured on the two-layer oxide and the 3D islands of the preparation shown in Fig. 6(b).

the rocksalt structure. The absence of strong density-of-states effects in STM images of the wurtzite phase, as compared to the first-layer moiré, might be related to the absence of a well-developed bandgap in wurtzite CoO, in contrast to the rocksalt structure.[46]

Scanning tunneling spectroscopy (STS)[47] curves obtained on two regions of the sample in Fig. 6(b), i.e., on top of the 2-ML islands and on the 3D oxide layer, are shown in Fig. 7. To avoid excessive noise in the bandgap, where $I \approx 0$ and thus ln I is a very high negative number, we do not display the unmodified normalized conductance, d ln I/d ln V but rather $(dI/dV)/(I/V + \varepsilon)$ with a small $\varepsilon = 10$ pA/V. The curves show a bandgap in the 3D islands between -0.4 and $+0.5$ V, whereas the first-layer (not shown) and second-layer moiré structures are still metallic. The gap in bulk CoO is larger, $\sim$3 eV.[48]

E. Surface alloy oxides

The results discussed in the previous paragraphs highlight the role of the interface interaction in the oxide morphology and show that excess Co above the first-layer completion results in Stranski-Krastanov growth. Therefore, the use of a surface alloy as a Co *reservoir* looks appealing for growing flat surface oxides. It is well known that annealing a Co ultrathin film deposited on Pt(111) above 670 K results in a Pt-rich surface alloy, which is terminated by a Pt-rich layer.[49,50] Under oxidizing conditions, the Co amount required for growing an oxide layer can migrate to the surface.

We evaporated 6 ML Co on Pt(111) at RT and annealed it at 740 K. Finally, 50 L of O_2 were dosed at 640 K. STM measurements (Fig. 8(a)) show an almost flat surface over hundreds of nanometers, with roughly triangular depressions, appearing $\sim$70 pm deep in the surface. Atomically resolved images (inset on the right side of the figure) show that the matrix is the clean metal (probably mostly Pt; we have not achieved chemical contrast in these areas), whereas the darker regions correspond to the moiré phase (inset on the left). Its appearance at different voltages (not shown) is the same as for the 1-ML-thick oxide films (Fig. 3). STS does not show a bandgap, as observed for thicker oxides, and the lattice constant suggests that it is a single CoO layer: an analysis of the dislocation pattern weakly visible in the images suggests

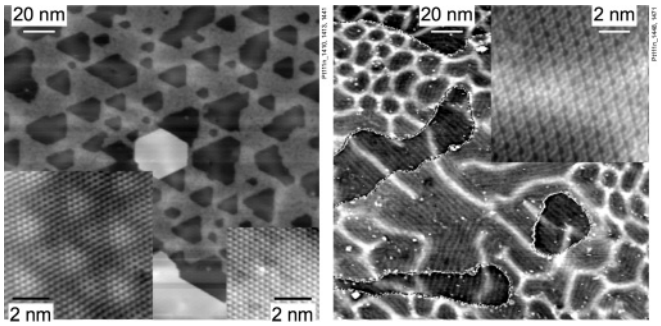

FIG. 8. (a) STM images of 6 ML Co/Pt(111) annealed at 740 K and then oxidized at 640 K ($V_s = +1$ V, $I_t = 0.1$ nA). The insets on the left and right sides show a zoom in the dark triangles ($V_s = +50$ mV, $I_t = 0.1$ nA) and in the matrix ($V_s = -1$ mV, $I_t = 2.5$ nA), respectively. (b) STM images of 3 ML Co/Pt(111) annealed and dosed at 640 K ($V_s = -1$ V, $I_t = 0.1$ nA). Image processing was used for better visibility of low-corrugation features on terraces, causing the noisy appearance of the steps. The inset shows a high-resolution image ($V_s = 2$ mV, $I_t = 1$ nA).

that the alloy substrate has $\sim$272 pm interatomic distance, and the STM images show that the oxide has a lattice constant 1.126 times that of the substrate, i.e., $\sim$306 pm for the oxide lattice, reasonably close to the value of 309 pm found for the oxide after deposition of 1 ML Co.

F. The quasi-(3 × 3) surface

We also studied oxidation of a surface with a higher Co concentration in the near-surface layers, obtained by annealing at a lower temperature of 640 K.[51] In this case, 3 ML Co were evaporated at RT, annealed at 640 K, and finally dosed with 50 L O_2 at this same temperature (Fig. 8(b)). Apart from bright subsurface dislocation lines due to the lattice misfit between the Pt substrate and the PtCo alloy, we found a flat homogeneous surface over several tens of nanometers. We also observed three rotational domains of a grating structure with a corrugation of $\sim$10 pm and periodicity of $\sim$3.3 nm. High-resolution images (inset in the figure) show that the surface is nanostructured with holes, forming a superstructure with a periodicity close to (3 × 3), confirmed by LEED; we therefore named it a quasi-(3 × 3) structure. We interpret this phase as the result of the oxidation of a Co-rich surface on top of the alloy. The same quasi-(3 × 3) phase was also observed after deposition of 2 ML Co, which was deposited at RT, annealed first and then dosed with 50 L O_2 at 570 K, and finally dosed with 2 L at 740 K (Fig. 9(a)). A third route toward preparation of this structure is deposition of 7 ML Co onto the 1-ML moiré in 10^{-7} mbar O_2 at 740 K; all these methods result in a Pt-Co alloy in the uppermost layers. When grown by the second method (2 ML Co annealed at 570 K and then at 740 K in oxygen), the quasi-(3 × 3) superstructure coexists with the moiré phase, which grows preferentially close to steps and with a high density of triangular dislocation loops.

A careful analysis of the STM images allows us to determine the exact unit cell of the quasi (3 × 3) structure with respect to the PtCo alloy. In the following, we assume that the alloy has the lattice constant of pure Pt; the actual values might be slightly lower due to the smaller alloy lattice constant. The

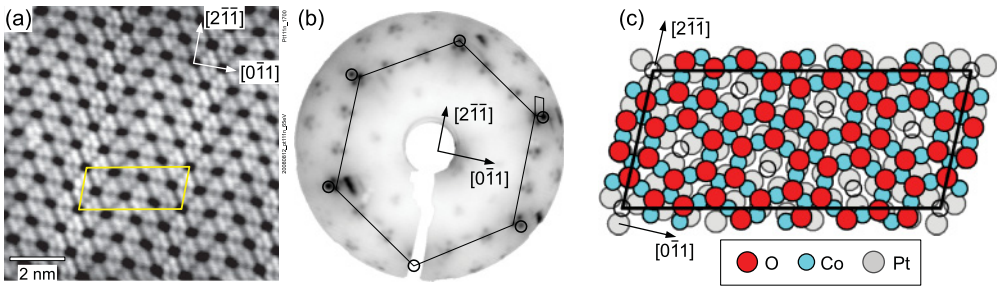

FIG. 9. (Color online) The quasi-(3 × 3) phase: (a) STM image ($V_s = -2$ mV, $I_t = 0.1$ nA). (b) LEED pattern at 65 eV with the substrate spots marked by circles and a large hexagon showing the expansion in the [0$\bar{1}$1] direction. (c) Structure model. The superstructure cell is marked in all frames.

lattice match is exact only in the fcc [2$\bar{1}$ $\bar{1}$] direction, with the spacing between the dark spots measured as 1.45 ± 0.01 nm in this direction, which compares well with $3 \times \sqrt{3} \times d_{\mathrm{Pt}} =$ 1.442 nm. In the [0$\bar{1}$1] direction, the oxide layer is expanded by ∼10% compared to an ideal (3 × 3) superstructure; the spacing between the dark holes being 0.92 ± 0.01 nm instead of $3 \times d_{\mathrm{Pt}} = 0.833$ nm. This is close to the misfit between the Pt and CoO lattice constants and is responsible for the ∼3.3-nm periodicity of the grating mentioned earlier. This periodicity is also seen in atomically resolved images as a weak modulation of contrast (Fig. 9(a)) and allows us to determine the exact unit cell, which is described by the matrix $\left(\begin{smallmatrix} 13 & 3 \\ 3 & 6 \end{smallmatrix}\right)$. Hence, the unit vectors of the superstructure cell are $|a_{S1}| = \sqrt{139} d_{\mathrm{Pt}} = 3.272$ nm, which fits the experimental value of ∼3.3 nm, and $|a_{S2}| = 1.442$ nm. This structure can also be described by a centered rectangular cell, $(23 \times 3\sqrt{3})$ − rect. The superstructure is also visible in LEED (Fig. 9(b)). There, the expansion manifests itself as inward movement of four of the six main spots (the hexagon in Fig. 9(b)); all spots appear as triplets due to the three different rotational domains.

Assuming that our STM shows the oxygen atoms as on all other Co oxides, we arrive at the structural model shown in Fig. 9(c). This structure is similar to the (3 × 3) structure observed by Knudsen *et al.*[38] for oxidized iron on Pt(111), but the deviation from the perfect (3 × 3) superstructure was not reported in that work. The Co layer is almost pseudomorphic to the substrate but expanded along [0$\bar{1}$1], with 21 Co-Co distances corresponding to 23 Pt-Pt ones ($d_{\mathrm{Co\text{-}Co}} = 304$ pm). On this structure, triangles of 3 O atoms have two orientations, which would correspond to fcc and hcp sites on a perfect (3 × 3) superstructure. We might think of these triangles as miniature versions of the triangular dislocation loops discussed in Sec. III B. Due to the expansion in the [0$\bar{1}$1] direction, exact fcc and hcp stacking is found only at the left and right sides of the unit cell; in the rest of the cell, the stacking is between these two extremes. Thus, the unfavorable hcp stacking is not avoided in this structure. The other type of unfavorable stacking, Co on top of Pt, is avoided by keeping commensurability along [2$\bar{1}$ $\bar{1}$]. In agreement with what has been discussed for the other first-layer oxides, the oxygen triangles with perfect fcc stacking show the strongest atomic contrast in STM.

We cannot directly determine whether the Co atoms drawn as open circles in Fig. 9(c), each surrounded by six oxygen triangles, are present or not. If present, these atoms would have no oxygen atom binding to them and could be Pt (which has a weaker affinity for oxygen than Co). The STM images show a dark hole at these positions, but the depression appears only ∼40 pm deep, much less than the geometric depth of a monolayer-deep hole. We consider it likely that a metal atom at this position would appear as a protrusion in STM, because the first-layer oxide appears darker than a Pt monolayer (Fig. 8(a)). Also, in a few STM images (not shown), we have observed some "holes" replaced by protrusions, indicating that an atom can indeed bind there and appear bright. We therefore consider it likely that this atom is missing in the usual quasi-(3 × 3) superstructure, as already proposed by Knudsen *et al.* for the FeO_x/Pt(111) case.[38] Finally, we also observed small patches of the (2 × 2) cobalt oxide phase, similar to that of iron oxide reported by Knudsen *et al.*[38] (not shown).

IV. CONCLUSION

We have shown that oxidation of Co films deposited on Pt(111) results in several phases with different morphology, depending on the preparation method, the film thickness, and the annealing temperature before and during oxygen dosing. Deposition of 1 ML of Co and subsequent O_2 dosing in the temperature range between RT and ∼470 K results in a rough surface. This is explained by an excess of Co, which is expelled from the almost pseudomorphic Co/Pt (111) layer during the oxide growth. A flat and almost flawless moiré pattern is obtained with oxidation at two increasing temperatures (570 and 740 K) of a 1-ML-thick Co deposit. At the final temperature, excess Co can diffuse into bulk. This shows that the moiré is the thermodynamically stable 2D cobalt oxide phase on Pt(111). AES and the striking analogy to the well-known FeO/Pt(111) case allow us to assign this moiré structure to an oxygen-terminated CoO(111) bilayer. The in-plane distance is slightly expanded (309 pm) compared to a truncated CoO(111) crystal (301 pm). This is probably associated with an out-of-plane contraction, which would reduce the surface dipolar energy. Although we did not find evidence for a bandgap in STS, the STM images of the moiré structure strongly depend on the tunneling voltage, which is more typical for semiconductors than for a metal. Interestingly, the two-layer moiré structure has an even larger in-plane lattice constant (315 pm). Thus, we believe that it has the wurtzite structure, with the Co of the upper bilayer on

top of the O atoms of the lower bilayer (Fig. 6(d)), similar to CoO/Ir(100).[19]

Insufficient oxidation of a single Co layer, whether deposited at rather low temperatures or derived from a near-surface PtCo alloy, leads to various substoichiometric structures. In the sequence of decreasing oxygen content, these are the moiré structure with dislocation triangles, the zigzag structure, and the quasi-(3 × 3) structure; the final one is obtained from near-surface PtCo alloys. With decreasing oxygen content, the Co-Co interatomic distance decreases, but even in the quasi-(3 × 3) structure with a stoichiometry of $CoO_{0.75}$ it is still higher than in bulk Pt (277.5 pm) and much higher than in bulk Co (250.7 pm). The dislocation triangles and the zigzag structure allow the system to avoid unfavorable stacking sequences of the upper three layers (Pt-Co-O). The quasi-(3 × 3) structure, having the lowest oxygen content of all, does not avoid the unfavorable Pt-Co-O hcp stacking. The zigzag structure is more effective in this respect, avoiding both Co-on-top-of-Pt and Pt-Co-O hcp stacking.

Both the first- and the second-layer moiré structures might find applications as templates for growing metal nanostructures. Applications involving noble metals seem more promising than attempts to deposit more reactive transition metals, which would tend react with the oxygen and destroy the moiré pattern. Nevertheless, a similar FeO/Pt(111) moiré has been recently used for growing fairly regularly arranged Fe and V clusters[11]; self-assembling arrays of gold adatoms on this substrate[12] show much better order, however. To our knowledge, the impact of deviations from the perfect moiré (triangular dislocation loops and zigzag phase) on metal nucleation has not been investigated so far on any similar oxide. Because we might expect the regular defects to act as nucleation centers, these surfaces look highly promising as templates.

Thicker films of CoO on Pt(111) grow in the Stranski-Krastanov mode, which becomes increasingly pronounced with increasing deposition and annealing temperature. The Stranski-Krastanov mode cannot be avoided by cycles of Co deposition and oxidation at elevated temperature. In agreement with the threefold symmetry of the 3D islands in these films, surface x-ray diffraction measurements, following step-by-step growth at 450 K, show that the island structure agrees well with the bulk CoO(111) rocksalt structure, in orientational epitaxy with the substrate.[42] As expected for CoO, the 3D nanoislands are semiconducting as shown by STS, though with a smaller bandgap than the bulk material. Considering the importance of the interface in exchange bias structures, a careful analysis of the CoO films like the one in the present study is clearly required for all work where CoO films or CoO-NiO combinations are used as antiferromagnetic materials for such applications.

Finally, sputter-cleaned STM tips consistently show the oxygen, not the metal atoms as protrusions in all of these structures, where a complete or almost complete close-packed oxygen layer is at the surface (at low coverages, oxygen usually appears as a depression in STM). The same was reported for various O/Rh structures,[34,52] and we consider it likely that this may be a rule for STM images of oxygen on the late transition metals.

ACKNOWLEDGMENTS

This work was supported by the Austrian Fonds zur Förderung der wissenschaftlichen Forschung.

*maurizio.de-santis@grenoble.cnrs.fr

[1] E. Lundgren, A. Mikkelsen, J. N. Andersen, G. Kresse, M. Schmid, and P. Varga, J. Phys. Condens. Matter **18**, R481 (2006).
[2] U. Diebold, S.-C. Li, and M. Schmid, Annu. Rev. Phys. Chem. **61**, 129 (2010).
[3] A. E. Berkowitz and K. Takano, J. Magn. Magn. Mater. **200**, 552 (1999).
[4] W. H. Meiklejohn and C. P. Bean, Phys. Rev. **102**, 1413 (1956).
[5] V. Skumryev, S. Stoyanov, Y. Zhang, G. Hadjipanayis, D. Givord, and J. Nogués, Nature **423**, 850 (2003).
[6] M. Gruyters and D. Riegel, Phys. Rev. B **63**, 052401 (2000).
[7] J. A. Borchers, M. J. Carey, R. W. Erwin, C. F. Majkrzak, and A. E. Berkowitz, Phys. Rev. Lett. **70**, 1878 (1993).
[8] J. M. Tonnerre, M. De Santis, S. Grenier, H. C. N. Tolentino, V. Langlais, E. Bontempi, M. Garcia-Fernandez, and U. Staub, Phys. Rev. Lett. **100**, 157202 (2008).
[9] A. Buchsbaum, M. De Santis, H. C. N. Tolentino, M. Schmid, and P. Varga, Phys. Rev. B **81**, 115420 (2010), and references therein.
[10] S. Degen, C. Becker, and K. Wandelt, Faraday Discuss. **125**, 343 (2004).
[11] N. Berdunov, G. Mariotto, K. Balakrishnan, S. Murphy, and I. V. Shvets, Surf. Sci. **600**, L287 (2006).
[12] L. Giordano, G. Pacchioni, J. Goniakowski, N. Nilius, E. D. L. Rienks, and H.-J. Freund, Phys. Rev. Lett. **101**, 026102 (2008).
[13] E. Cavaliere, I. Kholmanov, L. Gavioli, F. Sedona, S. Agnoli, G. Granozzi, G. Barcaro, and A. Fortunelli, Phys. Chem. Chem. Phys. **11**, 11305 (2009).
[14] S. Hayazaki, T. Matsui, H. Zhang, W. Chen, A. Wee, and J. Yuhara, Surf. Sci. **602**, 2025 (2008).
[15] J. W. Tasker, J. Phys. C **12**, 4977 (1979).
[16] J. Goniakowski, F. Finocchi, and C. Noguera, Rep. Prog. Phys. **71**, 016501 (2008).
[17] C. Noguera, J. Phys. Condens. Matter **12**, R367 (2000).
[18] D. Wolf, Phys. Rev. Lett. **68**, 3315 (1992).
[19] W. Meyer, D. Hock, K. Biedermann, M. Gubo, S. Müller, L. Hammer, and K. Heinz, Phys. Rev. Lett. **101**, 016103 (2008).
[20] O. Dulub, U. Diebold, and G. Kresse, Phys. Rev. Lett. **90**, 016102 (2003).
[21] W. Hebenstreit, M. Schmid, J. Redinger, R. Podloucky, and P. Varga, Phys. Rev. Lett. **85**, 5376 (2000).
[22] C. Noguera and J. Goniakowski, J. Phys. Condens. Matter **20**, 264003 (2008).
[23] M. Hassel and H.-J. Freund, Surf. Sci. **325**, 163 (1995).
[24] W. Meyer, K. Biedermann, M. Gubo, L. Hammer, and K. Heinz, Phys. Rev. B **79**, 121403(R) (2009).
[25] L. Gragnaniello, S. Agnoli, G. Parteder, A. Barolo, F. Bonbino, F. Allegretti, S. Surnev, G. Granozzi, and F. P. Netzer, Surf. Sci. **604**, 2002 (2010).

[26]S. Entani, M. Kiguchi, and K. Saiki, Surf. Sci. **566–568**, 165 (2004).
[27]C. Nagl, O. Haller, E. Platzgummer, M. Schmid, and P. Varga, Surf. Sci. **321**, 237 (1994).
[28]E. Lundgren, B. Stanka, M. Schmid, and P. Varga, Phys. Rev. B **62**, 2843 (2000).
[29]E. Lundgren, B. Stanka, W. Koprolin, M. Schmid, and P. Varga, Surf. Sci. **423**, 357 (1999).
[30]H. C. Galloway, J. J. Benitez, and M. Salmeron, Surf. Sci. **298**, 127 (1993).
[31]H. C. Galloway, P. Sautet, and M. Salmeron, Phys. Rev. B **54**, R11145 (1996).
[32]M. Ritter, W. Ranke, and W. Weiss, Phys. Rev. B **57**, 7240 (1998).
[33]Y. J. Kim, C. Westphal, R. X. Ynzunza, H. C. Galloway, M. Salmeron, M. A. Van Hove, and C. S. Fadley, Phys. Rev. B **55**, R13448 (1997).
[34]J. Gustafson, A. Mikkelsen, M. Borg, E. Lundgren, L. Köhler, G. Kresse, M. Schmid, P. Varga, J. Yuhara, X. Torrelles, C. Quirós, and J. N. Andersen, Phys. Rev. Lett. **92**, 126102 (2004).
[35]Scientific Group Thermodata Europe (SGTE), P. Franke, D. Neuschütz, *Landolt-Börnstein—Numerical Data and Functional Relationships in Science and Technology*, Group IV, Volume 19B (Springer, Berlin, 2004).
[36]L. Giordano, G. Pacchioni, J. Goniakowski, N. Nilius, E. D. L. Rienks, and H.-J. Freund, Phys. Rev. B **76**, 075416 (2007).
[37]L. R. Merte, J. Knudsen, L. C. Grabow, R. T. Vang, E. Lægsgaard, M. Mavrikakis, and F. Besenbacher, Surf. Sci. **603**, L15 (2009).
[38]J. Knudsen, L. R. Merte, L. C. Grabow, F. M. Eichhorn, S. Porsgaard, H. Zeuthen, R. T. Vang, E. Lægsgaard, M. Mavrikakis, and F. Besenbacher, Surf. Sci. **604**, 11 (2010).
[39]O. Dulub, W. Hebenstreit, and U. Diebold, Phys. Rev. Lett. **84**, 3646 (2000).
[40]D. R. Jennison, O. Dulub, W. Hebenstreit, and U. Diebold, Surf. Sci. **492**, L677 (2001).
[41]F. Sedona, G. Granozzi, G. Barcaro, and A. Fortunelli, Phys. Rev. B **77**, 115417 (2008).
[42]M. De Santis, H. C. N. Tolentino, J. M. Tonnerre, A. Bailly, and M.-C. Saint Lager, *ECSCD 9 (9th European Conference on Surface Crystallography and Dynamics)* (Vienna, 2–5 Sept. 2007).
[43]L. P. Zhang, J. van Ek, and U. Diebold, Phys. Rev. B **57**, R4285 (1998); **59**, 5837 (1999).
[44]J. Schoiswohl, S. Surnev, M. Sock, S. Eck, M. G. Ramsey, F. P. Netzer, and G. Kresse, Phys. Rev. B **71**, 165437 (2005).
[45]A. S. Risbud, L. P. Snedeker, M. M. Elcombe, A. K. Cheetham, and R. Seshadri, Chem. Mater. **17**, 834 (2005).
[46]T. Archer, R. Hanafin, and S. Sanvito, Phys. Rev. B **78**, 014431 (2008).
[47]R. M. Tromp, J. Phys. Condens. Matter **1**, 10211 (1989).
[48]V. I. Anisimov, M. A. Korotin, and E. Z. Kurmaev, J. Phys. Condens. Matter **2**, 3973 (1990).
[49]M. C. Saint-Lager, R. Baudoing-Savois, M. De Santis, and P. Dolle, Y. Gauthier, Surf. Sci. **418**, 485 (1998).
[50]Y. Gauthier, M. Schmid, S. Padovani, E. Lundgren, V. Buš, G. Kresse, J. Redinger, and P. Varga, Phys. Rev. Lett. **87**, 036103 (2001).
[51]R. Baudoing-Savois, P. Dolle, Y. Gauthier, M. C. Saint-lager, M. De Santis, and V. Jahns, J. Phys. Condens. Matter **11**, 8355 (1999).
[52]L. Köhler, G. Kresse, M. Schmid, E. Lundgren, J. Gustafson, A. Mikkelsen, M. Borg, J. Yuhara, J. N. Andersen, M. Marsman, and P. Varga, Phys. Rev. Lett. **93**, 266103 (2004).